

1 **Supporting Information for**
2 **“Seasonal variation in the correlation between anomalies of sea level and**
3 **chlorophyll in the Antarctic Circumpolar Current”**

4 **Hajoon Song¹, Matthew C. Long², Peter Gaube³, Ivy Frenger⁴, John Marshall¹, Dennis J.**
5 **McGillicuddy Jr.⁵**

6 ¹Department of Earth, Atmospheric and Planetary Sciences, Massachusetts Institute of Technology, Cambridge,

7 Massachusetts, USA

8 ²Climate and Global Dynamics Laboratory, National Center for Atmospheric Research, Boulder, Colorado, USA

9 ³Applied Physics Laboratory, University of Washington, Seattle, Washington, USA

10 ⁴GEOMAR Helmholtz Center for Ocean Research Kiel, Kiel, Germany

11 ⁵Department of Applied Ocean Physics and Engineering, Woods Hole Oceanographic Institution, Woods Hole,

12 Massachusetts, USA

13 This document provides supplementary information describing the methods used in
14 this study as well as additional figures and tables substantiating statements made in the
15 main article.

16 **Contents**

17	Satellite Observations	1
18	Model Simulation	2
19	Evaluation of the Model Simulation	4
20	Robustness of the seasonality in ρ_{SSH}, CHL'	4
21	The Fe budget averaged over the mixed layer	5
22	Iron supply by advection	6
23	Statistics	6
24	References	7

25 **Satellite observations**

26 We used the absolute dynamic topography mapped on $1/4^\circ \times 1/4^\circ$ grid from Collecte
27 Localis Satellites / Archiving, Validation and Interpretation of Satellite Oceanographic

Corresponding author: H. Song, hajsong@mit.edu

28 data (CLS/AVISO). The absolute dynamic topography data spans 10 years from 1998
 29 to 2007 at 7-day interval. The sea surface height (SSH) anomaly fields were then com-
 30 puted from this weekly data by spatially high-pass filtering with a half-power cutoff of 6°
 31 in both latitude and longitude.

32 Near-surface chlorophyll (CHL) concentration product comes from the Sea-Viewing
 33 Wide Field-of-View Sensor (SeaWiFS) project during the same period as the SSH anomaly.
 34 The Garver-Siegel-Maritorena (GSM) semi-analytical ocean color algorithm [*Garver and*
 35 *Siegel, 1997; Maritorena et al., 2002; Siegel et al., 2002*] was used to estimate CHL from
 36 ocean color measurements made by SeaWiFS. The log-transformed 9-km resolution daily
 37 CHL concentration estimates were averaged within the $1/4 \times 1/4$ degree grid to match the
 38 resolution of the SSH anomaly fields. This daily CHL data was merged to create data
 39 with 7-day interval to match the frequency of SSH anomaly fields using a loess filter with
 40 a half-power cutoff of 35-days (equivalent to a running mean with approximately a 20-day
 41 span) to remove temporal variability in the CHL measurements that are not captured in
 42 the SSH anomaly fields. This smoothing in time attenuates variability with wavelengths
 43 shorter than approximately 1 month, thus attenuating much of the submesoscale variabil-
 44 ity. This procedure was based on the detailed analysis of the AVISO SSH fields presented
 45 in Appendix A of *Chelton et al. [2011]*. The resulting CHL (and also SSH) fields can
 46 resolve mesoscale features with radii of approximately 50 km [*Chelton et al., 2011*]. Fi-
 47 nally, the high-pass filtering with a spatial loess smoother with a half-power cutoff of 6° in
 48 both latitude and longitude was used to compute the anomaly which was transformed back
 49 to linear concentrations [*Campbell, 1995; Gaube et al., 2013*]. The resultant smoothed
 50 CHL fields have spatial and temporal resolution comparable with the SSH anomaly fields.
 51 The Pearson correlation between anomalies of SSH and CHL ($\rho_{SSH,CHL}$) was com-
 52 puted for each grid box as shown in Figures 1a,b. In addition, we computed $\rho_{SSH,CHL}$
 53 in SSH bins, *i.e.* approximately along streamlines as shown in Figure 2a (see also *Frenger*
 54 [*2013*]).

55 **Model Simulation**

56 The mechanisms generating observed $\rho_{SSH,CHL}$ were examined using the Biogeo-
 57 chemical Elemental Cycling (BEC) model [*Moore et al., 2002, 2004, 2013*] coupled to
 58 the ocean circulation component of the Community Earth System Model (CESM) with a
 59 resolution of 0.1° (less than 10 km in zonal direction in the Drake Passage). Prior to this

simulation, the 0.1° physical model has run for 15 years and provides the initial conditions for the physical-biogeochemical coupled simulation. The GLObal Ocean Data Analysis Project (GLODAP) and World Ocean Atlas (WOA) climatology data were used for the initial condition for long-lived pools (e.g. dissolved inorganic carbon, alkalinity and nutrients) while other biogeochemical variables were integrated from the solution of 1° model. The total CHL concentration at any given depth is computed as the sum of CHL of three phytoplankton functional groups whose biomasses are affected by the uptake of varied nutrients including iron, and grazing by zooplankton. The vertical mixing is estimated by the K-Profile Parameterization (KPP) mixing scheme [Large *et al.*, 1994]. This scheme computes the depth of planetary boundary layer or vertical-mixing depth using a Richardson number criterion. This depth is generally shallower than that determined by hydrographic properties (e.g., potential density) because the latter one may include a region below the mixing layer reminiscent of the previous mixing. In this study, we referred to the depth of the mixing layer as the mixed-layer depth (MLD) in the analysis because the vertical mixing for tracers such as iron is subject to the vertical mixing scheme, which is the relevant metric for the budget analysis of iron over the mixing depth. The model simulates the depth attenuation of photosynthetically active radiation (PAR) on the basis of CHL concentration following [Morel and Maritorena, 2001].

Phytoplankton growth rates in the ocean biogeochemistry component of the CESM are computed as

$$\mu_i = \mu_{i,ref} \cdot T_f \cdot V_i \cdot L_i \quad (1)$$

where μ_i is the C-specific growth rate (d^{-1}) for phytoplankton functional type (PFT) i , $\mu_{i,ref}$ is the maximum growth rate (referenced to 30°C), and T_f is the temperature limitation (“Q10”) function; V_i and L_i are the nutrient and light response functions, respectively [Geider *et al.*, 1998]. For diatoms (diat), diazotroph (diaz) and “small” phytoplankton (sp), the nutrient response function follows Liebig’s law of the minimum, such that the ultimate limitation term used to compute growth is that of the most limiting nutrient:

$$V_{diat} = \min(V_{diat}^N, V_{diat}^P, V_{diat}^{Fe}, V_{diat}^{Si}) \quad (2)$$

$$V_{diaz} = \min(V_{diaz}^P, V_{diaz}^{Fe}) \quad (3)$$

$$V_{sp} = \min(V_{sp}^N, V_{sp}^P, V_{sp}^{Fe}) \quad (4)$$

The model was integrated for 5 years archiving 5-day means. The simulated SSH anomalies were computed as the observations; using a high-pass loess smoother with a

88 half-power cutoff of 6° [Chelton and Schlax, 2003]. The procedure for the CHL anomaly
 89 computation follows that used in the satellite data but from simulated 5-day mean total
 90 CHL concentrations near the surface. For Figures 1 and 2, the solutions were mapped to
 91 the same grid as the satellite SSH anomalies using a bilinear interpolation before comput-
 92 ing the correlation.

93 **Evaluation of the Model Simulation**

94 The eddy-rich 0.1° CESM has an SSH variability that agrees well with that esti-
 95 mated from space. Figure S1(a) shows the standard deviation of SSH in the observation
 96 from CLS/AVISO. The model simulation captures not only the observed spatial pattern
 97 of elevated SSH variability but also its magnitude, with regions of elevated SSH variabil-
 98 ity along the Antarctic Circumpolar Current (ACC), Brazil-Malvinas Confluence, Agulhas
 99 Current retroflexion and East Australian Current (Figure S1(b)). The simulated CHL near
 100 the surface agrees with SeaWiFS observations to a somewhat lesser degree than SSH vari-
 101 ability. Although the model underestimates the CHL concentration, it generally reproduces
 102 enhanced productivity near the shelf regions and islands, as well along the ACC as sug-
 103 gested by satellite observations. The depth of the mixed-layer estimated using potential
 104 density ($\Delta\rho = 0.03 \text{ kg m}^{-3}$) in the model is also comparable with that in the observations
 105 from Dong *et al.* [2008] based on Argo float profiles (Figure S2). The non-uniformity
 106 of the depth of mixed-layer along the ACC in winter is represented by the model. The
 107 simulated iron also captures a large scale iron distribution in observations taken from the
 108 dataset by Tagliabue *et al.* [2012] (Figure S3).

109 **Robustness of the seasonality in $\rho_{SSH',CHL'}$**

110 The $\rho_{SSH',CHL'}$ was evaluated using 95% confidence interval from Fisher transfor-
 111 mation. The seasonality of the $\rho_{SSH',CHL'}$ characterized by the opposite sign in different
 112 seasons remains along the ACC within the 95% confidence interval (Figure S4(a-d)). We
 113 also evaluated the robustness of the seasonality of $\rho_{SSH',CHL'}$ using the rank correlation.
 114 As shown in Figure S4(e,f), $\rho_{SSH',CHL'}$ along the ACC is generally positive in summer
 115 but negative in winter similar to Figure 1. Hence the seasonality in $\rho_{SSH',CHL'}$ is robust.

116 The $\rho_{SSH',CHL'}$ in the model has the upper and lower limits of the 95% confidence
 117 levels that are similar to Figure 1(c,d) and not shown here. The seasonality of the $\rho_{SSH',CHL'}$

118 in the model is also robust as the rank correlation shows the coefficients that seasonally
 119 change signs along the ACC (not shown).

120 The Fe budget averaged over the mixed layer

121 We analyzed the budget of iron ($Fe(z, t)$) averaged over the mixed layer $H(t) = \eta(t) -$
 122 $h(t)$, where $\eta(t)$ is the SSH and $h(t)$ is the time-varying MLD. The temporal evolution of
 123 the iron averaged over the mixed layer ($\langle Fe \rangle \equiv \frac{1}{H(t)} \int_{h(t)}^{\eta(t)} Fe(z, t) dz$) can be written as

$$\begin{aligned} \frac{d\langle Fe \rangle}{dt} &= \frac{d}{dt} \left[\frac{1}{H(t)} \right] \int_{h(t)}^{\eta(t)} Fe(z, t) dz + \frac{1}{H(t)} \int_{h(t)}^{\eta(t)} \frac{d}{dt} Fe(z, t) dz \\ &+ \frac{1}{H(t)} \left[Fe(\eta(t), t) \frac{d\eta(t)}{dt} - Fe(h(t), t) \frac{dh(t)}{dt} \right] \\ &= \frac{1}{H(t)} \int_{h(t)}^{\eta(t)} \frac{d}{dt} Fe(z, t) dz \\ &+ \frac{1}{H(t)} \left[(Fe(\eta(t), t) - \langle Fe \rangle) \frac{d\eta(t)}{dt} - (Fe(h(t), t) - \langle Fe \rangle) \frac{dh(t)}{dt} \right]. \end{aligned} \quad (5)$$

124 The first term in (5) represent the iron tendency averaged over the MLD and the remain-
 125 ing terms are the contribution by entrainment/detrainment.

126 The $Fe(z, t)$ tendency in the model is computed as follows:

$$\begin{aligned} \frac{d}{dt} Fe(z, t) &= -A_h(z, t) - \frac{\partial}{\partial z} (w(z, t) Fe(z, t)) + \frac{\partial}{\partial z} \left(\kappa(z, t) \frac{\partial Fe(z, t)}{\partial z} \right) \\ &+ F(z, t) + B(z, t), \end{aligned} \quad (6)$$

where A_h is the horizontal advection, w is the vertical velocity, $\kappa(z, t)$ is the vertical dif-
 fusivity, $F(z, t)$ is the surface iron flux (nonzero only at the surface) and $B(z, t)$ is the bi-
 ological source/sink term. The right-hand-side terms in (6) are computed using the 5-day
 mean model output, while the left-hand-side term is estimated using a centered difference
 approximation over 10 days. Using (6), (5) can be written as

$$\begin{aligned} \frac{d\langle Fe \rangle}{dt} &= \frac{1}{H(t)} \int_{h(t)}^{\eta(t)} \left[-A_h(z, t) - \frac{\partial}{\partial z} (w(z, t) Fe(z, t)) \right] dz && \text{[3D adv]} \\ &- \frac{1}{H(t)} \kappa(h(t), t) \frac{\partial Fe(z, t)}{\partial z} \Big|_{z=h} && \text{[v. mix]} \\ &+ \frac{1}{H(t)} \int_{h(t)}^{\eta(t)} F(z, t) dz && \text{[s. flux]} \\ &+ \frac{1}{H(t)} \int_{h(t)}^{\eta(t)} B(z, t) dz && \text{[bio]} \\ &+ \frac{1}{H(t)} \left[(Fe(\eta(t), t) - \langle Fe \rangle) \frac{d\eta(t)}{dt} - (Fe(h(t), t) - \langle Fe \rangle) \frac{dh(t)}{dt} \right] && \text{[ent]} \end{aligned} \quad (7)$$

127 with the surface value of the diffusivity, $\kappa(\eta(t), t) = 0$. The meaning of each label are as
 128 follows: “3D adv: 3-dimensional advection”, “v. mix: vertical mixing”, “s. flux: aeolian

129 input of dust”, “bio: biological source/sink and scavenging” and “ent: entrainment associ-
130 ated with MLD changes”.

131 **Iron supply by advection**

132 The contribution from advection, including eddy-driven lateral advection via trap-
133 ping and stirring, potentially plays a role regionally if iron concentrations increase equator-
134 ward (i.e., warm anticyclonic features with anomalously high iron concentration and cold
135 cyclonic features with lower iron concentration). The Atlantic Ocean sector has a clear in-
136 creasing equatorward trend of iron concentration in observations [Mawji *et al.*, 2015], i.e.
137 sufficiently large to make an effect. Yet, in the Indian and Pacific Ocean sectors, small
138 meridional gradients in iron are reported in the spring/summer vertical section of iron
139 from GEOTRACES Intermediate Data Product 2014 [Mawji *et al.*, 2015].

140 The simulated iron in the model exhibits similar lateral gradient as observations. In
141 summer (January-March, Figure S5(top)), the Indian-Pacific sector has little meridional
142 gradient of surface iron as iron is depleted by active primary production, which makes it
143 unlikely that lateral advection by, e.g., stirring and trapping are driving the iron anomaly
144 in Fig 4a. In the Atlantic sector, however, iron concentration generally increases equator-
145 ward. Consistent with *in situ* observations [Bowie *et al.*, 2002], iron is supplied from the
146 Patagonian Shelf to the northern ACC creating a meridional gradient in the model. With
147 iron concentrations increasing toward the equator, eddy-driven advection as well as verti-
148 cal mixing, can create iron perturbations associated with eddies.

149 In winter (July-September), the surface ocean features a higher iron concentration
150 than in summer (Figure S5(bottom)). The primary productivity is more regulated by light
151 availability, nevertheless the wintertime iron distribution shows how closely iron is linked
152 to the vertical mixing, especially in the Indian-Pacific sector. There, deeper vertical mix-
153 ing enriches the surface ocean with iron as indicated by the fact that higher concentration
154 of iron collocates with the region of relatively deep mixed layers (> 50 m). The MLD in
155 the Indian-Pacific sector is spatially inhomogeneous with larger horizontal iron gradients
156 in winter than in summer. As a result, it is more likely that the eddy-driven advection sets
157 the perturbations in iron, but vertical mixing modulation becomes larger than in summer
158 at the same time. The meridional gradient of Fe in the Atlantic sector shows no seasonal-
159 ity.

Statistics

We constructed distributions of $\langle \text{Fe} \rangle$, $\langle \text{PAR} \rangle$ and the terms in (7) at the locations of anticyclones and cyclones in summer and winter along the ACC. Since not all distributions are normally distributed (e.g. $\langle \text{Fe} \rangle$), the median is used as a representative measure of the distributions. Medians of $\langle \text{Fe} \rangle$ and $\langle \text{PAR} \rangle$ distributions for anticyclones and cyclones in the ACC are first obtained. Then the differences in medians between anticyclones and cyclones are normalized by the median for the entire ACC to measure the relative size of those differences. In Figures 4a,c, we plot the percent value of the median differences. The terms in (7) are normalized by the median of $\langle \text{Fe} \rangle$ along the entire ACC after being multiplied by 10 days, the time interval used in the tendency equation in the model. We then compare the medians of each term to quantify the systematic differences between anticyclones and cyclones in Figures 4b,d in the main article.

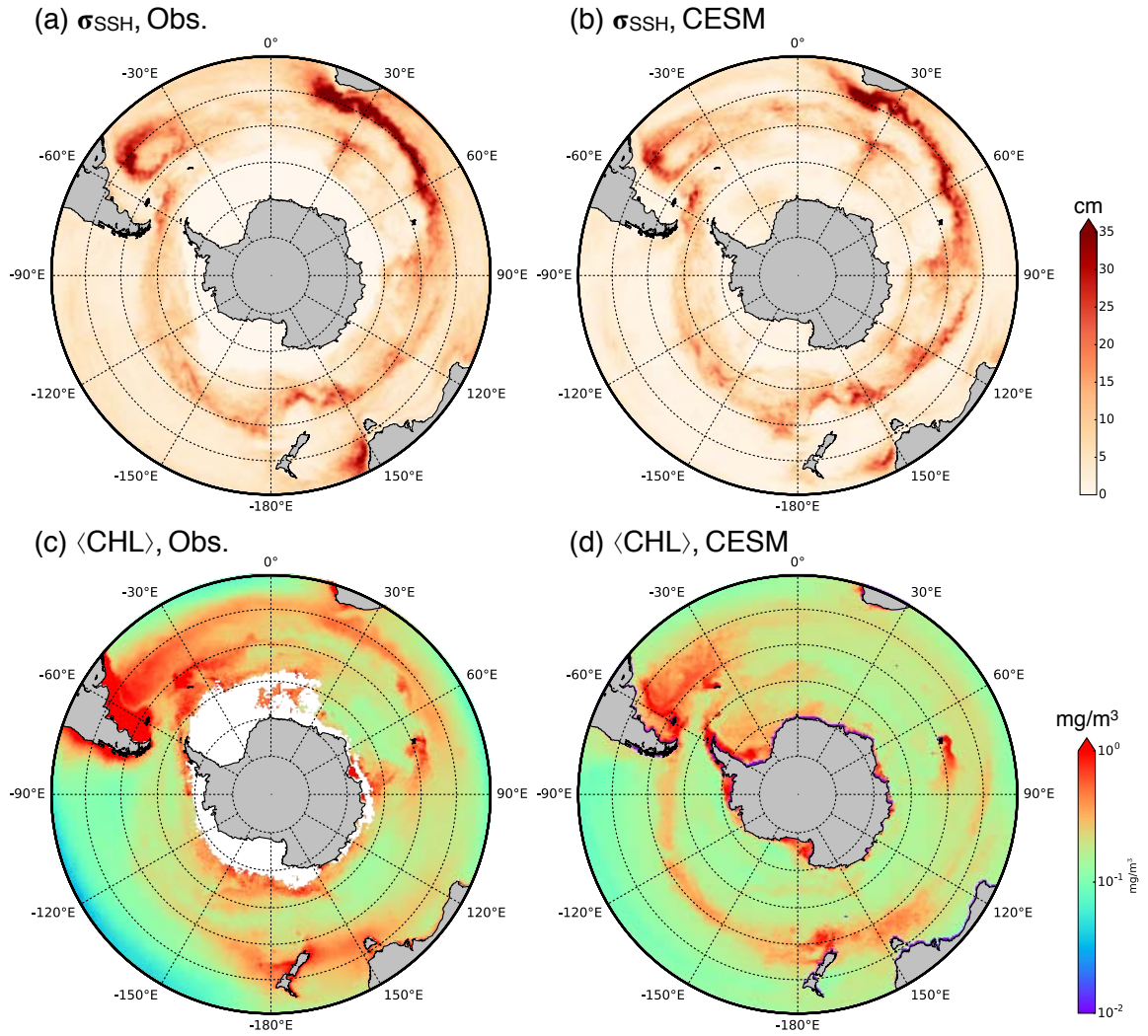
The 95% confidence intervals are estimated using a bootstrap test where we randomly subsampled the data ($O(10^6)$) and obtained a median value. By repeating this resampling procedure 100 times, the 95% confidence interval can be estimated from the distribution of medians. Since the 95% confidence intervals are too narrow to be visible, they are not plotted in Figures 3 and 4.

References

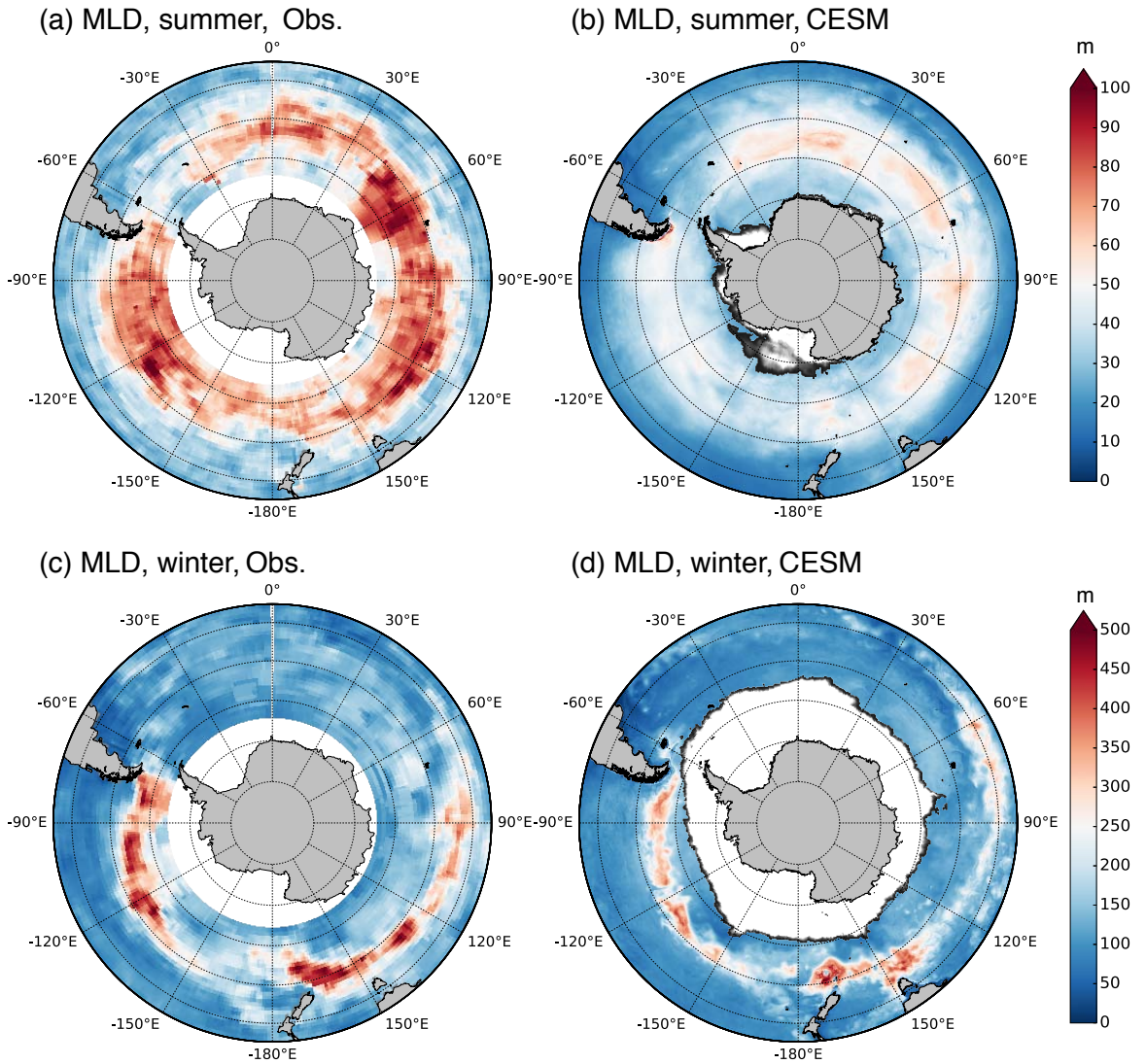
- Bowie, A., D. Whitworth, E. Achterberg, R. Mantoura, and P. Worsfold (2002), Biogeochemistry of Fe and other trace elements (Al, Co, Ni) in the upper Atlantic Ocean, *Deep-Sea Res. Pt I*, 49(4), 605–636.
- Campbell, J. W. (1995), The lognormal distribution as a model for bio-optical variability in the sea, *J. Geophys. Res.*, 100(C7), 13,237–13,254, doi:10.1029/95JC00458.
- Chelton, D. B., and M. G. Schlax (2003), The accuracies of smoothed sea surface height fields constructed from tandem satellite altimeter datasets, *J. Atmos. Oceanic Technol.*, 20, 1276–1302.
- Chelton, D. B., M. G. Schlax, and R. M. Samelson (2011), Global observations of nonlinear mesoscale eddies, *Prog. Oceanogr.*, 91(2), 167–216, doi: <http://dx.doi.org/10.1016/j.pocean.2011.01.002>.
- Dong, S., J. Sprintall, S. T. Gille, and L. Talley (2008), Southern Ocean mixed-layer depth from Argo float profiles, *J. Geophys. Res.*, 113, C06,013.

- 191 Frenger, I. (2013), On Southern Ocean eddies and their impacts on biology and the atmo-
192 sphere, Ph.D. thesis, ETH Zurich, Zurich, Switzerland, doi:10.3929/ethz-a-009938120.
- 193 Garver, S. A., and D. A. Siegel (1997), Inherent optical property inversion of ocean color
194 spectra and its biogeochemical interpretation: 1. time series from the sargasso sea, *J.*
195 *Geophys. Res. Oceans*, *102*(C8), 18,607–18,625, doi:10.1029/96JC03243.
- 196 Gaube, P., D. B. Chelton, P. G. Strutton, and M. J. Behrenfeld (2013), Satel-
197 lite observations of chlorophyll, phytoplankton biomass, and ekman pumping
198 in nonlinear mesoscale eddies, *J. Geophys. Res. Oceans*, *118*, 6349–6370, doi:
199 10.1002/2013JC009027.
- 200 Geider, R., H. MacIntyre, and T. Kana (1998), A dynamic regulatory model of phyto-
201 plankton acclimation to light, nutrients, and temperature, *Limnol. Oceanogr.*, *43*, 679–
202 694.
- 203 Large, W., J. McWilliams, and S. Doney (1994), Oceanic vertical mixing: A review and a
204 model with nonlocal boundary layer parameterization, *Rev. Geophys.*, *32*, 363–403.
- 205 Maritorena, S., D. A. Siegel, and A. R. Peterson (2002), Optimization of a semianalytical
206 ocean color model for global-scale applications, *Appl. Opt.*, *41*(15), 2705–2714, doi:
207 10.1364/AO.41.002705.
- 208 Mawji, E., et al. (2015), The GEOTRACES intermediate data product 2014, *Mar. Chem.*,
209 *177*, 1–8, doi:https://doi.org/10.1016/j.marchem.2015.04.005.
- 210 Moore, J. K., S. C. Doney, J. A. Kleypas, D. M. Glover, and I. Y. Fung (2002), An inter-
211 mediate complexity marine ecosystem model for the global domain, *Deep Sea Res., Part*
212 *II*, *49*(1-3), 403–462.
- 213 Moore, J. K., S. C. Doney, and K. Lindsay (2004), Upper ocean ecosystem dynamics
214 and iron cycling in a global three-dimensional model, *Global Biogeochem. Cycles*, *18*,
215 GB4028, doi:10.1029/2004GB002220.
- 216 Moore, J. K., K. Lindsay, S. C. Doney, M. C. Long, and K. Misumi (2013), Marine
217 ecosystem dynamics and biogeochemical cycling in the Community Earth System
218 Model [CESM1(BGC)]: Comparison of the 1990s with the 2090s under the RCP4.5
219 and RCP8.5 scenarios, *J. Clim.*, *26*(23), 9291–9312, doi:10.1175/JCLI-D-12-00566.1.
- 220 Morel, A., and S. Maritorena (2001), Bio-optical properties of oceanic waters: a reap-
221 praisal, *J. Geophys. Res.*, *106*(C4), 7163–7180, doi:10.1029/2000jc000319.
- 222 Siegel, D. A., S. Maritorena, N. B. Nelson, D. A. Hansell, and M. Lorenzi-Kayser (2002),
223 Global distribution and dynamics of colored dissolved and detrital organic materials, *J.*

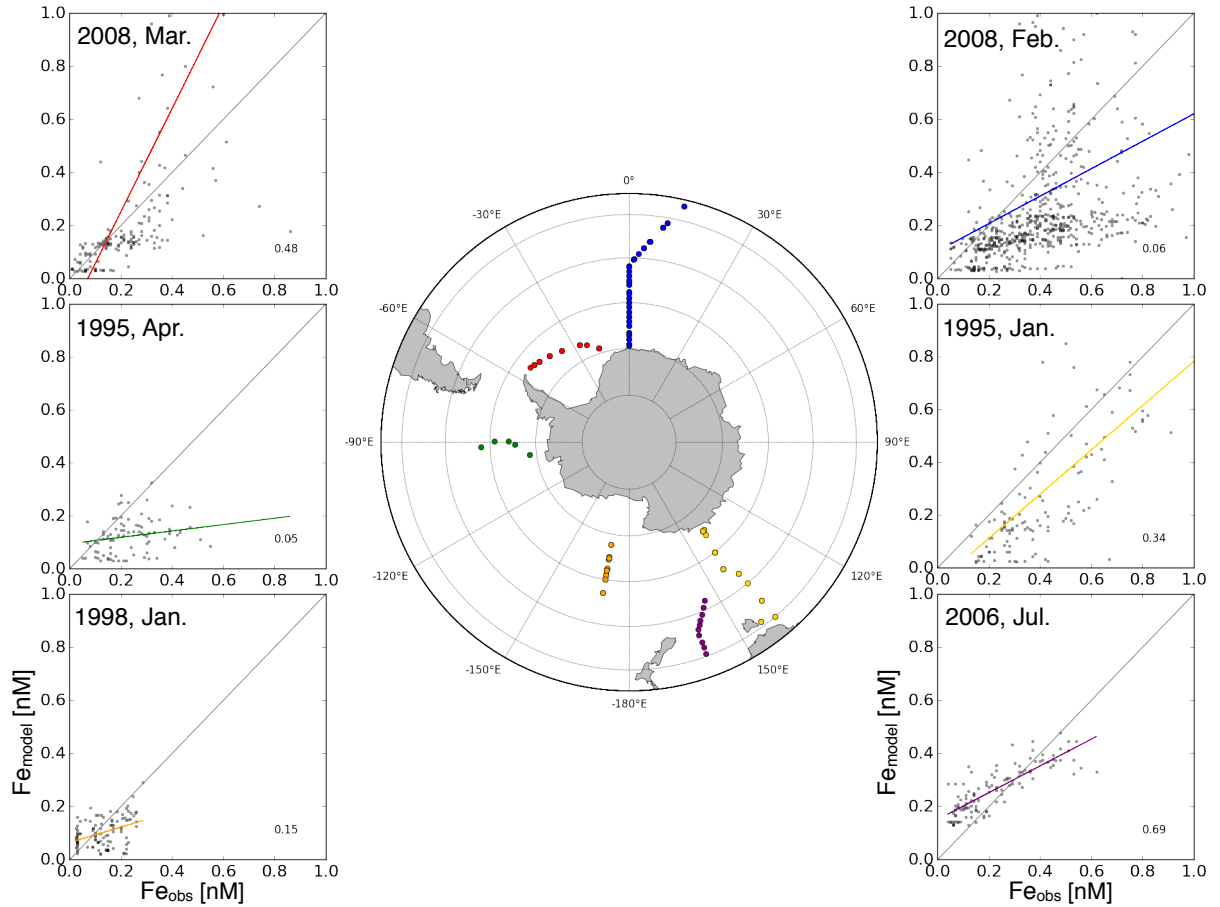
224 *Geophys. Res. Oceans*, 107(C12), 21–1–21–14, doi:10.1029/2001JC000965.
225 Tagliabue, A., T. Mtshali, O. Aumont, A. Bowie, M. Klunder, A. Roychoudhury, and
226 S. Swart (2012), A global compilation of dissolved iron measurements: focus on dis-
227 tributions and processes in the Southern Ocean, *Biogeosciences*, 9, 2333–2349, doi:
228 10.5194/bg-9-2333-2012.



229 **Figure S1.** Standard deviation of SSH from (a) satellite observation and (b) eddy-resolving CESM. (c) and
 230 (d) show the 10-year mean surface CHL estimated by ocean color and 5-year mean surface CHL from CESM,
 231 respectively. The white mask in (c) represents missing data.



232 **Figure S2.** The depth of the mixed-layer estimated using potential density. The potential density at this
 233 level is 0.03 kg m^{-3} greater than that at the surface. (a,b) are the average for austral summer (January-March)
 234 and (c,d) are the average MLD for austral winter (July-September). (a,c) are the MLD from *Dong et al.* [2008]
 235 and (b,d) are from CESM.



236 **Figure S3.** Dissolved iron concentration from observations and the model simulation is plotted along 6
 237 transects in the SO. The observational data is taken from *Tagliabue et al.* [2012]. The colored lines are the
 238 linear least squares fit between the observations and the model data (gray dots), while gray lines are the one
 239 with a slope of 1. R^2 values are provided at the right bottom corner of each panel. The colored dots on the
 240 map indicate the sampling location corresponding to the same colored line in the 6 panels.

Correlation between SSH' and CHL'

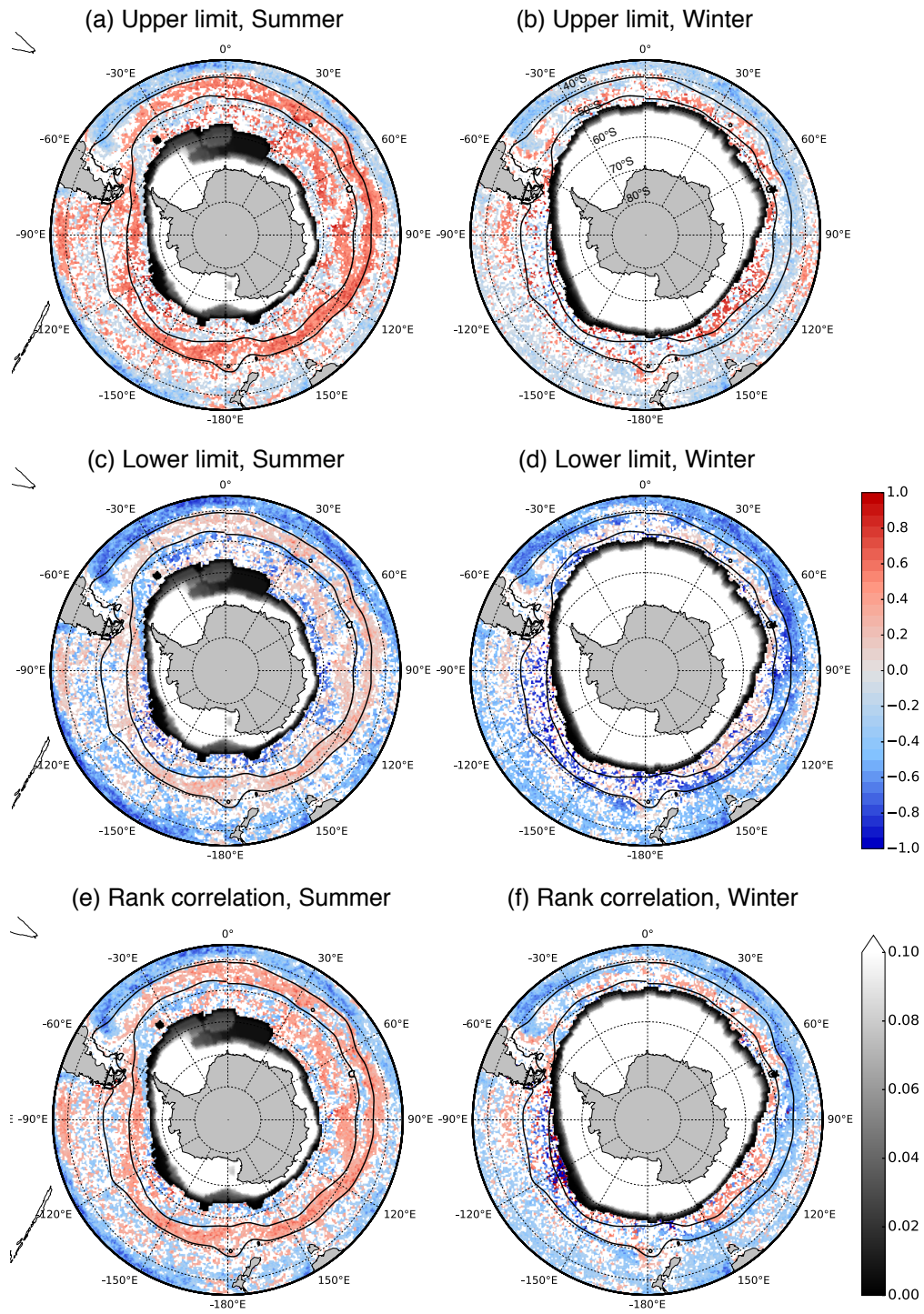
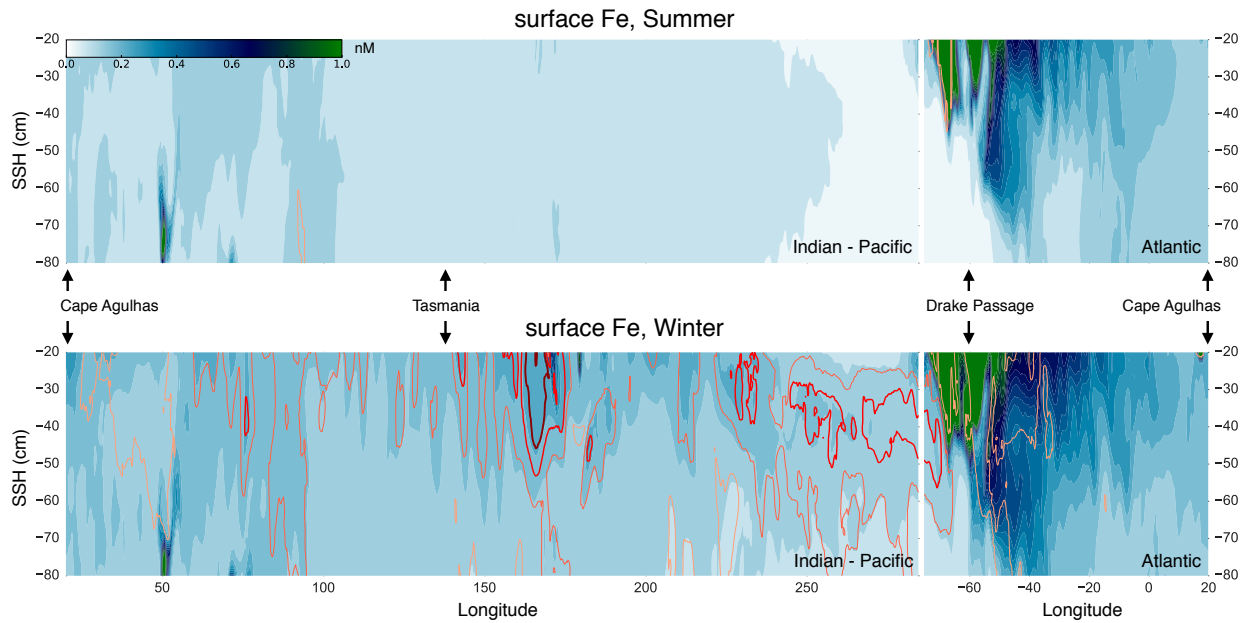


Figure S4. (Caption next page.)

242 **Figure S4.** (Previous page.) The (a,b) upper limit and (c,d) and lower limit of the 95% confidence intervals
 243 were estimated using Fisher transformation for the correlation coefficients between anomalies of SSH and
 244 CHL from satellite observations. Panels (e,f) are the rank correlation coefficients between anomalies of SSH
 245 and CHL from the same satellite observations. The panels (a,c,e) and (b,d,f) shows the correlation coefficients
 246 in austral summer (January-March) and winter (July-September), respectively.



247 **Figure S5.** The shading is the seasonal mean surface iron along the SSH isolines for austral (top) summer
 248 and (bottom) winter computed in CESM. Orange, pink, red and dark red contours represent MLD contours of
 249 50 m, 100 m, 150 m and 200 m, respectively.